ISSN 1674-1056
http://cpb.iphy.ac.cn
http://iopscience.iop.org/cpb
中国物理 B
Chinese Physics
中国物理
Chinese Physics B

Pair distribution function analysis: Fundamentals and application to battery materials

Xuelong Wang(王雪龙), Sha Tan(谭莎), Xiao-Qing Yang(杨晓青), Enyuan Hu(胡恩源)
Citation: Chin. Phys. B . 2020, 29(2): 028802 . **doi:** 10.1088/1674-1056/ab6656
Journal homepage: http://cpb.iphy.ac.cn; http://iopscience.iop.org/cpb

What follows is a list of articles you may be interested in

Advanced characterization and calculation methods for rechargeable battery materials in multiple scales

Xin-Yan Li(李欣岩), Su-Ting Weng(翁素婷), Lin Gu(谷林)
Chin. Phys. B . 2020, 29(2): 028801 . **doi:** 10.1088/1674-1056/ab65ba

Discovery and design of lithium battery materials via high-throughput modeling

Xuelong Wang(王雪龙), Ruijuan Xiao(肖睿娟), Hong Li(李泓), Liquan Chen(陈立泉)
Chin. Phys. B . 2018, 27(12): 128801 . **doi:** 10.1088/1674-1056/27/12/128801

High capacity sodium-rich layered oxide cathode for sodium-ion batteries

Gen-Cai Guo(郭根材), Changhao Wang(王长昊), Bang-Ming Ming(明帮铭), Si-Wei Luo(罗斯玮), Heng Su(苏恒), Bo-Ya Wang(王博亚), Ming Zhang(张铭), Hai-Jun Yu(尉海军), Ru-Zhi Wang(王如志)
Chin. Phys. B . 2018, 27(11): 118801 . **doi:** 10.1088/1674-1056/27/11/118801

All-solid-state lithium batteries with inorganic solid electrolytes: Review of fundamental science

Xiayin Yao(姚霞银), Bingxin Huang(黄冰心), Jingyun Yin(尹景云), Gang Peng(彭刚), Zhen Huang(黄祯), Chao Gao(高超), Deng Liu(刘登), Xiaoxiong Xu(许晓雄)
Chin. Phys. B . 2016, 25(1): 018802 . **doi:** 10.1088/1674-1056/25/1/018802

Scientific and technological challenges toward application of lithium-sulfur batteries

Ya-Xia Yin(殷雅侠), Hu-Rong Yao(姚胡蓉), Yu-Guo Guo(郭玉国)
Chin. Phys. B . 2016, 25(1): 018801 . **doi:** 10.1088/1674-1056/25/1/018801

TOPICAL REVIEW — Advanced calculation & characterization of energy storage materials & devices at multiple scale

Pair distribution function analysis: Fundamentals and application to battery materials

Xuelong Wang(王雪龙), Sha Tan(谭莎), Xiao-Qing Yang(杨晓青), and Enyuan Hu(胡恩源)†

Chemistry Division, Brookhaven National Laboratory, Upton 11973, *USA*

(Received 20 November 2019; revised manuscript received 29 December 2019; accepted manuscript online 31 December 2019)

Battery materials are of vital importance in powering a clean and sustainable society. Improving their performance relies on a clear and fundamental understanding of their properties, in particular, structural properties. Pair distribution function (PDF) analysis, which takes into account both Bragg scattering and diffuse scattering, can probe structures of both crystalline and amorphous phases in battery materials. This review first introduces the principle of PDF, followed by its application in battery materials. It shows that PDF is an effective tool in studying a series of key scientific topics in battery materials. They range from local ordering, nano-phase quantification, anion redox reaction, to lithium storage mechanism, and so on.

Keywords: battery materials, pair distribution function (PDF)

PACS: 88.80.ff **DOI:** 10.1088/1674-1056/ab6656

1. Introduction

Battery materials are indispensable to a clean and sustainable society.[1] Their importance has recently been acknowledged by the awarding of 2019 Nobel prize in chemistry.[2] While there is no doubt about their success, there are always strong motivations to make them better in terms of energy density, fast charging capability, and environmental friendliness. These improvements rely on a clear understanding of battery materials' fundamental properties, in particular, structural properties.[3]

Studying the structural properties of battery materials is by no means a trivial task as the materials themselves are intrinsically complicated. For example, the local structure can be diverse due to Jahn–Teller distortion,[4] cation ordering,[5] local distortion,[6] and so on. In addition, battery materials can be crystalline or amorphous, depending on performance optimization requirements. These facts pose grand challenges for a reliable characterization of battery materials. More challenging situations arise when it comes to studying how structures change in response to an external electric field as in the case of charging and discharging.[7]

Diffraction techniques including x-ray diffraction (XRD) and neutron diffraction (ND) are conventionally used to study the structural properties of materials. They are established on the basis of translational symmetry, or long-range order, and are very effective in elucidating the structures of crystals.[8–11] However, for materials without long-range order, such as nano and amorphous materials, the application of diffraction methods is very limited.[12–17] Such limitation is attributed to two facts. First, short-range structural information is embedded in the diffuse scattering.[18–23] Unfortunately, this part is usually either too weak to detect (orders of magnitude weaker than the Bragg scattering) or thrown away during background subtraction. As a result, short-range structural information is lost. Secondly, nano-phases give rise to very broad and weak Bragg peaks which can make phase quantification highly challenging if possible.[24,25]

In this context, total scattering technique that includes both Bragg scattering and diffuse scattering stand out as an effective tool to address the aforementioned scientific issues. Coupled with Fourier transform and pair distribution function (PDF) analysis, it helps to answer a series of questions regarding local structure, nano-phase quantification, anion redox reaction, and lithium storage mechanism.[26–35] In this review, principles of PDF will be explained, followed by the introduction of total scattering measurement instrumentation. After that, some representative cases in which PDF plays a key role in answering scientific questions are presented.

2. PDF fundamentals and total scattering experimental set-up

The PDF method originates from the Debye scattering equation developed by Debye back in 1915.[36] In 1927, Zernicke and Prins pointed out the Fourier relationship between the real-space atomic pair density and the Q space total scattering intensity.[37] Q is the scattering vector whose magnitude is $4\pi \sin\theta/\lambda$ (2θ is the scattering angle and λ is the incident radiation wavelength). While the mathematical foundations have been established a long time ago, PDF was not widely applied until recent decades. This is because to do a meaningful Fourier transform, total scattering data should cover a

†Corresponding author. E-mail: enhu@bnl.gov

© 2020 Chinese Physical Society and IOP Publishing Ltd

large range of Q. But both atomic form factor and atomic displacement parameter can lead to significant intensity decrease at high Q, making the data quality very poor in this region. Thanks to the advancement of modern x-ray synchrotron facility and spallation neutron sources, extremely high flux of x-ray photons and neutrons can be obtained. Coupled with high energy, or short wave-length λ, high Q region can now be accessed (since Q is inversely proportional to λ) and a high quality Fourier transform can be implemented. Here, some mathematical basics are explained and several functions are introduced. Some function has strict physical definition, such as $g(r)$; some have computational convenience, such as $G(r)$; and some provides intuitive understanding, such as $R(r)$. To begin with, the pair distribution function $g(r)$ is defined as follows:

$$g(r) = \frac{1}{4\pi\rho_0 r^2 N} \sum_i \sum_{j \neq i} \delta(r - r_{ij}),$$

in which ρ_0 is the average number density of atoms, N is the total number of atoms, and r_{ij} is the distance between atom i and atom j. $\delta(r - r_{ij})$ is the Dirac delta function which equals a single unit only when $r = r_{ij}$. In practice, the reduced atomic pair distribution function $G(r)$ is more frequently used,

$$G(r) = 4\pi r \rho_0 [g(r) - 1].$$

This is because $G(r)$ can be directly calculated from the measured total scattering function $S(Q)$ through Fourier transformation

$$G(r) = \frac{2}{\pi} \int_0^\infty Q[S(Q) - 1] \sin(Qr) \mathrm{d}Q,$$

where Q is the amplitude of the transferred momentum calculated by the difference between scattered wavevector and incident wavevector. $S(Q)$ by definition is calculated by measured coherent scattering intensity $I^{\mathrm{coh}}(Q)$

$$S(Q) = 1 + \frac{I^{\mathrm{coh}}(Q) - \sum c_i \left| f^i(Q) \right|^2}{\left| \sum c_i f^i(Q) \right|^2},$$

where c_i is the atomic concentration of the i-th type of elements and $f^i(Q)$ is its atomic x-ray scattering factor or neutron scattering length. The coherent scattering intensity $I^{\mathrm{coh}}(Q)$ can be directly collected from the experimentally measured total intensity $I(Q)$ when properly corrected for incoherent intensity, background noises, detector efficiency, multiple scattering, etc. By now, the relationship between measurable total scattering intensity $I(Q)$ and structural function $g(r)$ has been established. To better understand the meaning of $g(r)$, it is necessary to introduce the closely-related radial distribution function (RDF), $R(r)$, which offers a more intuitive picture:

$$R(r) = 4\pi r^2 \rho_0 g(r).$$

As shown in Fig. 1(a), $rR(r)$ indicates the number of atoms that can be found inside the spherical shell with radius r and thickness $\mathrm{d}r$ centering around another atom.[11] For detailed introduction on different correlation functions for describing the total scattering, interested readers could find a systematical review in which David A. Keen compared the commonly used correlation functions.[38]

Figure 1(b) shows a typical PDF pattern ($G(r)$) for a material. It is a real-space function and a wealth of structural information can be directly obtained from it. The peak position indicates the distance of atomic pairs. The area of peaks is related to the abundance of relevant pairs weighted by their scattering power. The width of peaks is related to disorder inside the material which can be structural disorder or/and atomic thermal vibration. The maximum distance at which peaks are observable gives insight to the size of coherent domain.[39,40]

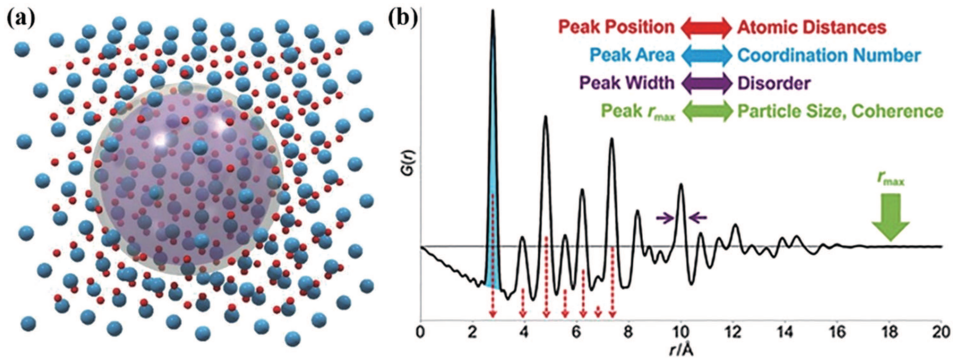


Fig. 1. (a) Atom distribution of CeO_2 in real space, and a sphere centered at an atom with radius r and annulus thickness $\mathrm{d}r$.[11] (b) High-energy x-ray total scattering derived pair distribution function in real space, $G(r)$, provides real-space structure information which is independent of structure modeling.[39]

For a successful total-scattering measurement, scattering data needs to cover a wide range of Q. Practically, this means a short wavelength is required for the experiment since Q is inversely proportional to λ. It also means a very high flux of radiation source is needed because both atomic form factor and structural disorder (including thermal vibration and static uncertainties) can lead to significant dampening in the high Q region. The former mostly influences x-ray experiment and the latter influences both x-ray and neutron experiments. Because of these considerations, PDF experiments are

mostly done at either x-ray synchrotron facilities or high flux neutron facilities (e.g., spallation neutron sources). It should also be noted that the diffuse scattering part is very important to PDF measurement and needs to be dealt with carefully. In diffraction experiment, this part of information is lost during background subtraction which is generally done by fitting a high order polynomial. In total scattering experiments, diffuse scattering is preserved in the total scattering data by measuring a separate background (including air scattering and sample container scattering) pattern which is subtracted from the sample's total scattering pattern. Such obtained data contains Bragg scattering, diffuse scattering, as well as inelastic scattering parts, which are all from the sample itself only. The inelastic part is further removed from the data in a PDF processing software such as PDFgetX3. Figures 2(a) and 2(b) schematically demonstrate the commonly used experimental set-ups for x-ray and neutron total-scattering measurements, respectively. For x-ray PDF experiments, a large 2D detector is placed behind the sample to collect the total scattering pattern. Considering the diffraction geometry, the detector needs to be very close to the sample to access the high Q region. The signal from the 2D image will be integrated into 1D total-scattering function data $S(Q)$ and further converted to PDF data through Fourier transformation. For neutron PDF experiments, the measurement is done in time-of-fly (TOF) style where the transferred momentum is calculated by the time difference between events of neutrons ejection and neutrons hitting on the detector.[41] As shown in Fig. 2(b), many banks of detectors are placed alongside the heading direction of the incident beams collecting the scattered neutrons.[42] The benefit of using neutron is that the neutron scattering length of elements is aperiodic and this provides the possibility of probing some light elements such as C, N, O, and F with high sensitivity. In contrast, the x-ray scattering power of an element is proportional to its atomic number and therefore low Z element has small scattering power. In the following case studies on battery materials, it will be shown that two PDF analysis methods are complementary to each other. Both of them play important roles in understanding the science in battery materials. The large area detector and high flux x-ray/neutron source used for total scattering experiments can help finishing data acquisition in a few seconds. The *in situ* total scattering experiment under conditions such as heating and battery cycling can be easily realized with properly designed sample stage and *in situ* cell. More information on the *in situ* total scattering experiments has been summarized in recent reviews.[7,43]

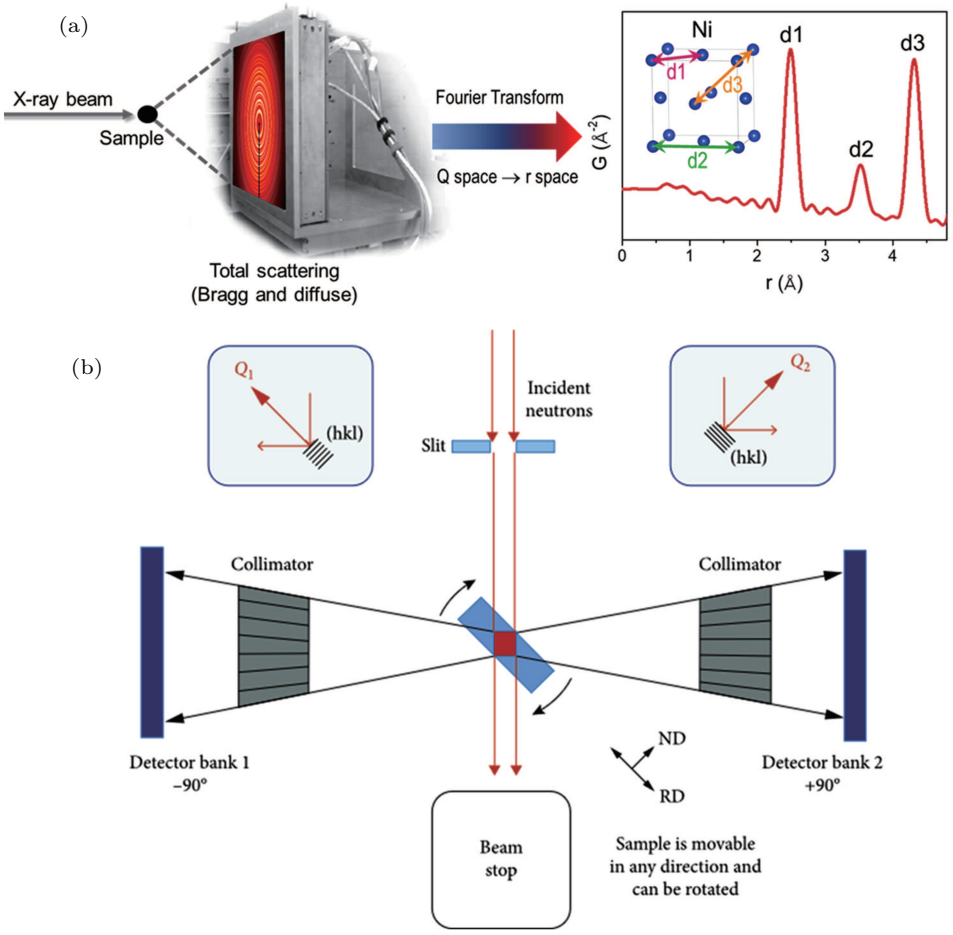


Fig. 2. (a) Transmission geometry set-up for modern x-ray pair distribution function measurements, where combination of high-energy x-ray and a large-area detector placed close to the sample could approach a wide Q range. The PDF data shown here, accompanied with its schematic structure, are for Ni with face-centered-cubic structure. (b) Schematic top view of time-of-flight neutron diffraction (TOF-ND) diffractometer and sample placement (not to scale).[42]

3. Application of PDF methods to battery materials

3.1. Reaction mechanism of nano-sized or amorphous electrode materials

Nano-particles and amorphous materials are commonly seen in battery materials. On the one hand, nanosizing is sometimes beneficial as it decreases the effective diffusion length and speeds up the electrochemical reaction. On the other hand, lithiation or sodiation can give rise to nano-sized or amorphous phases during the reaction. A typical example is conversion type materials, such as silicon anode and metal oxide/fluoride cathode. They are usually nano-sized in pristine state and can become amorphous during electrochemical reactions.[16,44,45] In these cases, the Bragg peaks (XRD) are either totally lost because of a lack of long-range ordering or are too broad and weak which denies a reliable structural analysis. PDF, as a total scattering technique, probes both the crystalline and amorphous phases effectively and plays a unique and important role in structural study of these battery materials.

The patterns shown in Fig. 3(a) are the *ex-situ* PDF of a silicon anode collected during the first discharge by Key *et al.*[46] It can be seen that during discharge, the peak intensities of all Si–Si pairs generally decrease. Specifically, the peaks at long distances decrease much faster than those at short distances (< 5 Å, corresponding to the Si–Si pairs in the first and second coordination shells). Upon discharging to 50 mV, all of the peaks above 4.5 Å essentially disappear. The total loss of atomic pairs at long distance implies almost complete amorphization of the silicon anode lattice at low voltage during deep lithiation. The PDF pattern of the fully discharged (0 mV) sample is fitted using the structure of $Li_{15}Si_4$, which is believed to be the main product of silicon lithiation. The result is shown in Fig. 3(b). The fitted curve and the measured data differ significantly below 3.8 Å but agree well above that. This indicates that the lithiation product of silicon contains considerable local disorder. Fitting is much improved when a nano-sized silicon is introduced as the secondary phase. More detailed analysis revealed the evolution of the silicon anode during electrochemical cycling as illustrated in Fig. 3(c). At the initial stage of discharge, lithiation begins close to the surface of small crystalline silicon particles and propagates towards the inner part with the breakage of Si–Si bonds, resulting in the formation of small Si clusters surrounded by Li ions. The competition between lithiation of small Si cluster and lithiation of remaining crystalline Si framework goes on for the whole discharge process until all silicon atoms from the lattice are consumed. Defected crystalline phase $Li_{15+\delta}Si_4$ may nucleate from the newly-formed amorphous phase. Upon first charging, delithiation of $Li_{15+\delta}Si_4$ phase proceeds from both the surface and the bulk area. The PDF results indicate that once nucleation sites of small Si clusters are formed, they begin to grow into an amorphous silicon matrix with few Li ions trapped inside. In the following discharging/charging cycles, Li ions insertion and extraction take place in the amorphous silicon phase instead of returning back to crystalline Si particles. Based on the understanding of the above mechanism, the authors suggested that the cycling potential window should be controlled for optimizing the reversibility and capacity retention of silicon anode.

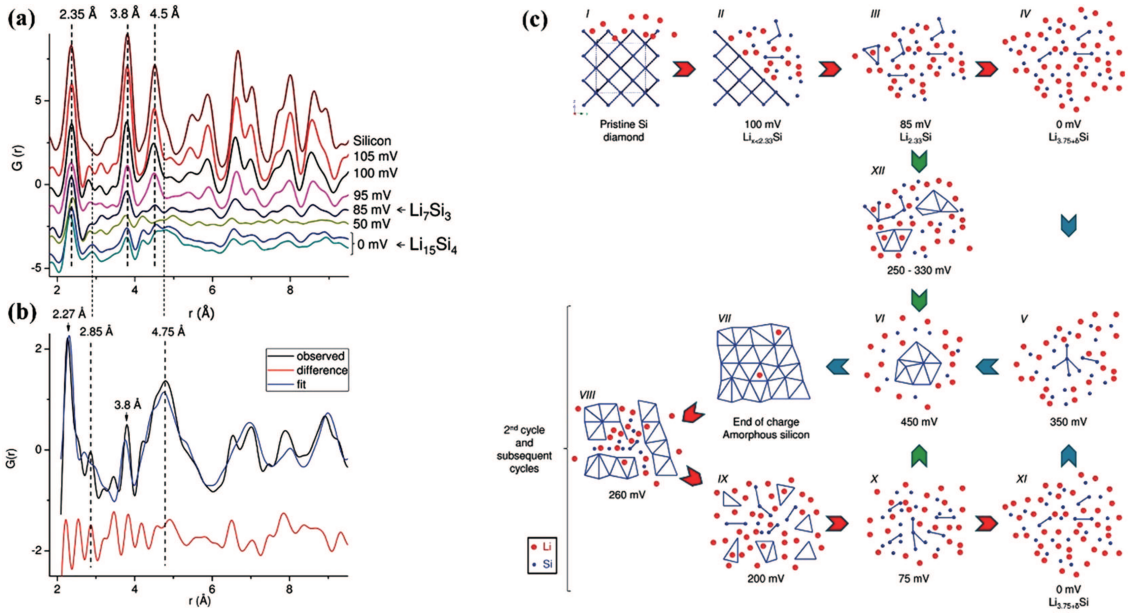


Fig. 3. (a) The *ex-situ* PDF of silicon extracted from the first discharge process. Dashed lines: the first, second, and third coordination shell Si–Si distances in a Si diamond framework. Two 0 mV samples are included, blue (top): the unwashed sample, teal (bottom): the washed sample. (b) PDF data and the fitting result ($R_w = 43\%$) of the washed 0 mV sample. Characteristic $Li_{15}Si_4$ correlations are indicated by the dashed lines at 2.85 Å and 4.75 Å, connecting (a) and (b). (c) Schematic illustration of silicon lithiation and delithiation. Crystalline silicon lithiation process (discharged down to 0 mV) corresponds I to IV. Discharge steps are denoted by red arrows, while blue and green arrows denote charge steps. Delithiation of fully lithiated silicon is shown by V to VIII, and VIII to XI correspond to the relithiation of amorphous silicon to form fully lithiated silicon for cycle number x ($x > 1$).[46]

Another attractive conversion material is FeF_3 and its various derivatives, which are low cost and environmentally benign. In addition, it can take up to 4 Li ions per formula and enable multiple electron transfer, promising a high energy density.[47] However, this material suffers from the problem of large voltage hysteresis and poor cyclability. To understand the reaction mechanism, Wiaderek *et al.* carried out *in situ* PDF experiment for FeO_xF_{1-x} (Fig. 4(a)).[48] PDF revealed the presence of an amorphous rutile phase that was difficult to be probed otherwise. The authors provided a quantitative description of the evolution of both crystalline and amorphous phases during charging/discharging (Fig. 4(b)). It is found that the highly reversible intercalation-extrusion reaction precedes the less reversible conversion reaction. Fan *et al.* proposed to use Co and O dual-doping in FeF_3 to decrease the voltage hysteresis and increase the cyclability.[49] Such strategy turned out to be very successful as indicated by the excellent electrochemical performance. PDF studies indicated that in the dual-doped samples, the reversible intercalation-extrusion reaction is greatly promoted and the irreversible conversion reaction is significantly suppressed. In details, figure 4(c) shows that each relevant phase has its own characteristic PDF peak and this provides a convenient and reliable way to analyze the phase composition. Figures 4(d) and 4(e) show the measured PDF patterns for $Fe_{0.9}Co_{0.1}OF$ and FeOF materials in both charged and discharged states after 100 cycles. The main difference between them is that in $Fe_{0.9}Co_{0.1}OF$ the intensity of the metal phase peak (around 2.5 Å) is much smaller than that in FeOF at the discharged state. Figure 4(f) shows the composition analysis of the two materials from fitting results. The proportion of the rocksalt phase in the final discharge products greatly increases after the introduction of dual doping. Therefore, the authors concluded that dual doping enhances the reversible extrusion reaction and suppresses the irreversible conversion reaction.

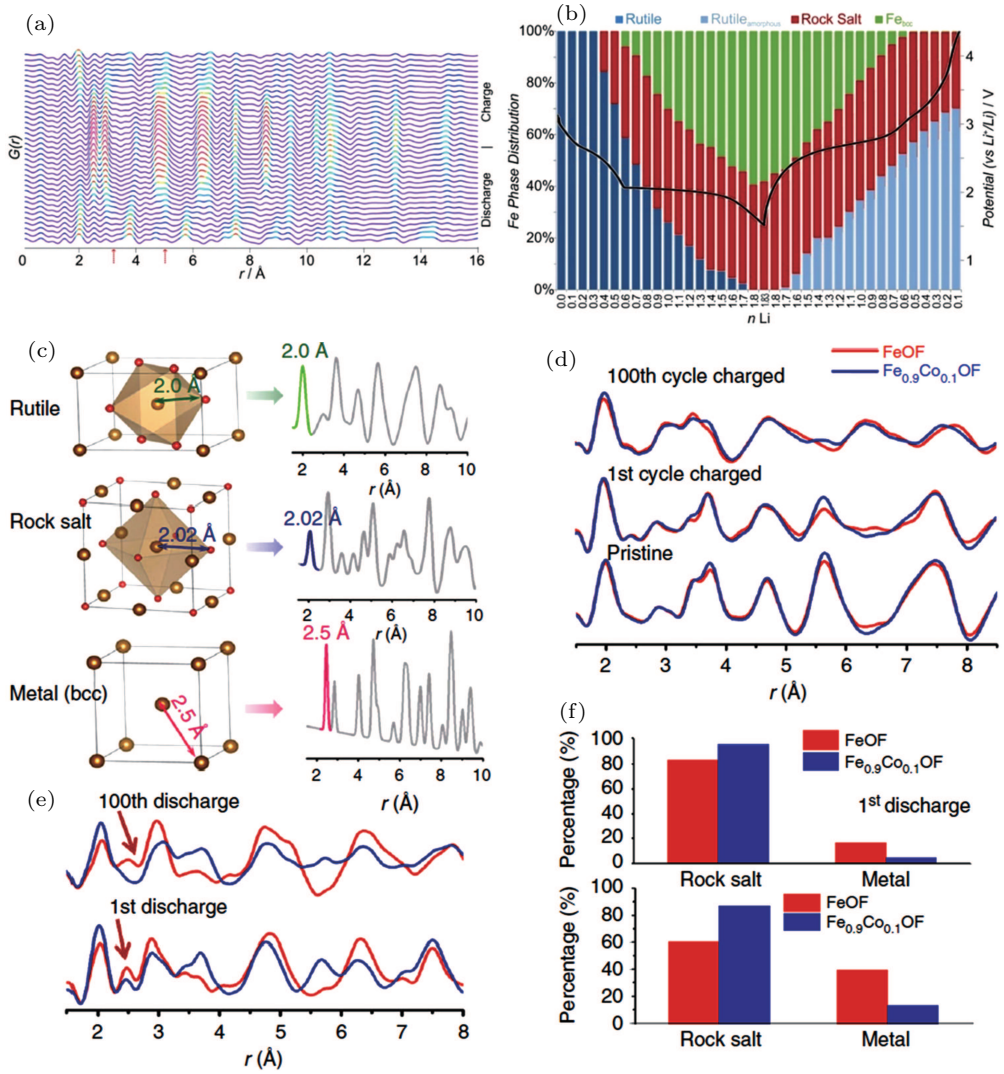


Fig. 4. (a) The *in situ* PDF data of iron oxyfluoride ($Fe^{II}_{(1-x)}Fe^{III}_xO_xF_{2-x}$, $x = 0.6$) during the first discharge–charge cycle. Characteristic peaks of the rock salt intermediate are indicated by arrows. Relative peak intensities are indicated by colors. (b) Evolution of phase composition in $Fe^{II}_{(1-x)}Fe^{III}_xO_xF_{2-x}$ ($x = 0.6$) during cycling. (c) Characteristic atomic pairs in rutile, rocksalt, and body-centered-cubic metal and their corresponding PDF peaks. (d) PDF patterns of $Fe_{0.9}Co_{0.1}OF$ and FeOF at pristine state, charged state after the 1st cycle, and charged state after the 100th cycle. (e) PDF patterns of $Fe_{0.9}Co_{0.1}OF$ and FeOF at discharged state after the 1st cycle and discharged state after the 100th cycle. (f) Percentages of metal and rocksalt phases in $Fe_{0.9}Co_{0.1}OF$ and FeOF obtained by fitting PDF results.[48,49]

3.2. Anion redox reaction mechanism in battery materials

Conventional battery materials are based on transition metal redox such as Co^{3+}/Co^{4+} and Ni^{3+}/Ni^{4+}. One possibility of increasing the energy density is to activate the oxygen anions and utilize the anion redox reaction.[50–53] To make such a reaction as reversible as possible, it is critical to understand the reaction mechanism. The O–O pair distance has been believed to be sensitive to oxygen anion redox and such information provides a very important piece in having a full picture of the reaction. Neutron PDF (nPDF) is particularly effective in probing this information for two reasons. First, PDF itself is a direct histogram of all the atomic pairs weighted by their scattering power and abundance. This is without the limitation of crystalline or amorphous phases. Second, oxygen has a large scattering length for neutron, meaning that oxygen-involved atomic pairs will be carrying a lot of weight in the nPDF pattern. Such technique has been recently applied to sodium-ion battery cathode materials such as $Na_{0.6}[Li_{0.2}Mn_{0.8}]O_2$ which is anion redox active and delivers very large capacity.[54]

Figure 5(a) shows the unit cell for the crystal structure of $Na_{0.6}[Li_{0.2}Mn_{0.8}]O_2$ material and the PDF data collected for its pristine and charged states. The $Na_{0.6}[Li_{0.2}Mn_{0.8}]O_2$ material has a so-called "layered P3" type crystal structure which means that Na^+ ions sit on the interlayer trigonal prismatic interstitial sites formed by the oxygen framework and there are three transition metal layers in a unit cell. The *in-operando* XRD measurement results show highly reversible features during cycling, which indicates the stability of global crystal structure against desodiation or sodiation. Furthermore, the P3 structure maintains throughout the charging and discharging processes, suggesting the rigidity of the oxygen framework. While little information is obtained from XRD as the long range average structure shows little change during electrochemical cycling, nPDF and x-ray PDF (xPDF) can provide a wealth of structural information. As can be seen in the upper panel of Fig. 5(a), nPDF peaks corresponding to atomic pairs Na–O, O–O, and Na–Mn can be directly identified. The most obvious difference between the patterns of the pristine state and the charged state is the new shoulder peak at ~ 2.5 Å in the charged one which is related to a shortened O–O pair. The lower panel of Fig. 5(a) shows the xPDF patterns. The peaks corresponding to the Mn–O and Mn–Mn pairs in close shell (< 4 Å) barely change after charging, implying that the local coordination environment of the transition metal mostly maintains, which is consistent with the XRD results. The more significant changes of PDF patterns at larger atomic pair distances after charging (for both nPDF and xPDF) turn out to be caused by stacking faults introduced by desodiation as the model structure in Fig. 5(d) illustrates. Using a structural model containing stacking faults, the authors carried out a co-refinement of total scattering data in reciprocal space (Fig. 5(b)) and PDF data in real space (Fig. 5(c)) for samples at the charged state. The results located the short and long O–O atomic pairs. The short O–O pair distance (~ 2.5 Å, suggestive of peroxo-like species) is related to the interlayer O–O pair while the long O–O pair (~ 2.8 Å) is related to the intralayer O–O pair which mostly stays the same during charging. Further nPDF refinement indicates the absence of transition metal migration and oxygen vacancies. Such analysis indicates that the P3-type lattice framework is fairly rigid and helps to promote the reversibility of the anion redox reaction.

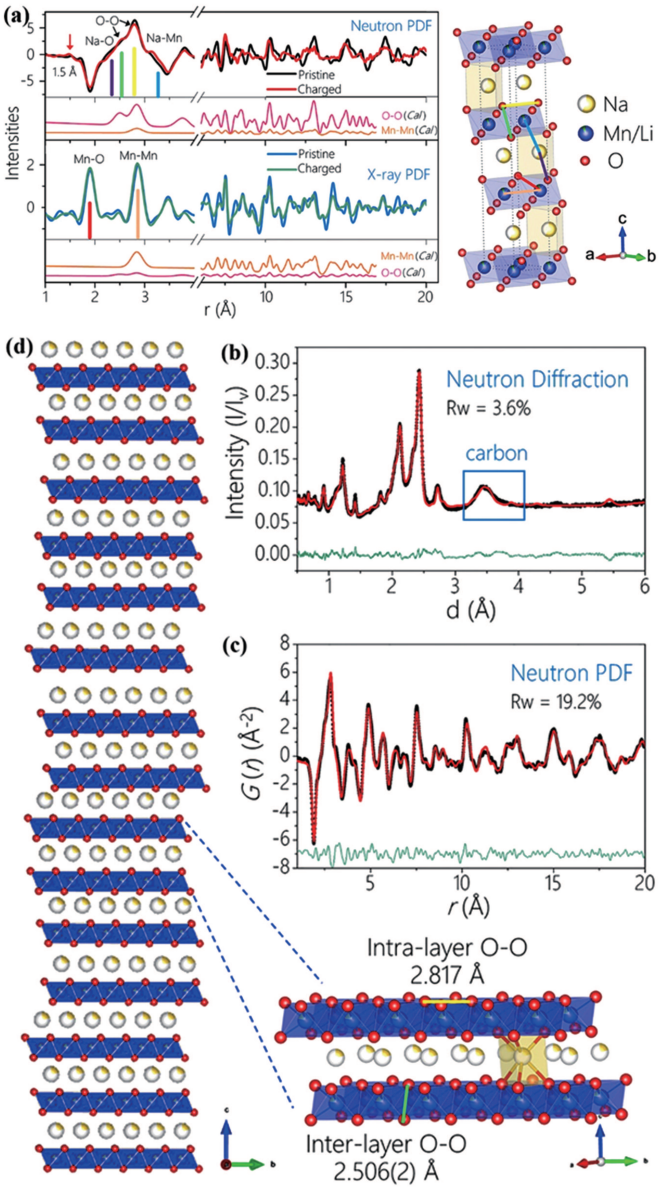


Fig. 5. (a) Local structural changes of $Na_{0.6}[Li_{0.2}Mn_{0.8}]O_2$ collected at pristine and charged state (4.5 V) are reflected in xPDF and nPDF with the first coordination bonding labeled. Refinement results of (b) the neutron diffraction data and (c) neutron PDF data using the supercell structural model in (d). (d) The refined 15-layer supercell model for the charged $Na_{0.2}[Li_{0.2}Mn_{0.8}]O_2$ (4.5 V). The enlarged figure shows the local coordination environments of O and residual Na.[54]

NPDF is also used to study the anion redox re-

action in the cation-disordered cathode material. Figure 6(a) shows the structure model and neutron powder diffraction pattern for cation-disordered cathode material $Li_{1.2}Ti_{0.35}Ni_{0.35}Nb_{0.1}O_{1.8}F_{0.2}$ (LTNNbOF) which is also anion redox active.[55] Figure 6(b) shows its nPDF pattern and the peaks for the nearest TM–O and O–O atomic pairs. Different from the case of $Na_{0.6}[Li_{0.2}Mn_{0.8}]O_2$ where O–O pairs are shortened during oxygen oxidation, the O–O pairs mostly maintain their distance in LTNNbOF as shown in Fig. 6(c). This is also verified by scanning transmission electron microscopy (STEM) results (Figs. 6(d) and 6(e)). Further analysis reveals that cation disordering greatly reduces the possibility of forming coplanar O 2p orbital pair which is needed for the O–O pair shortening as observed in other anion redox active materials. From these cases, it can be seen that nPDF provides a direct local probe to specific O–O atomic pairs. For the anion redox reaction study, nPDF is a very valuable structural characterization tool.

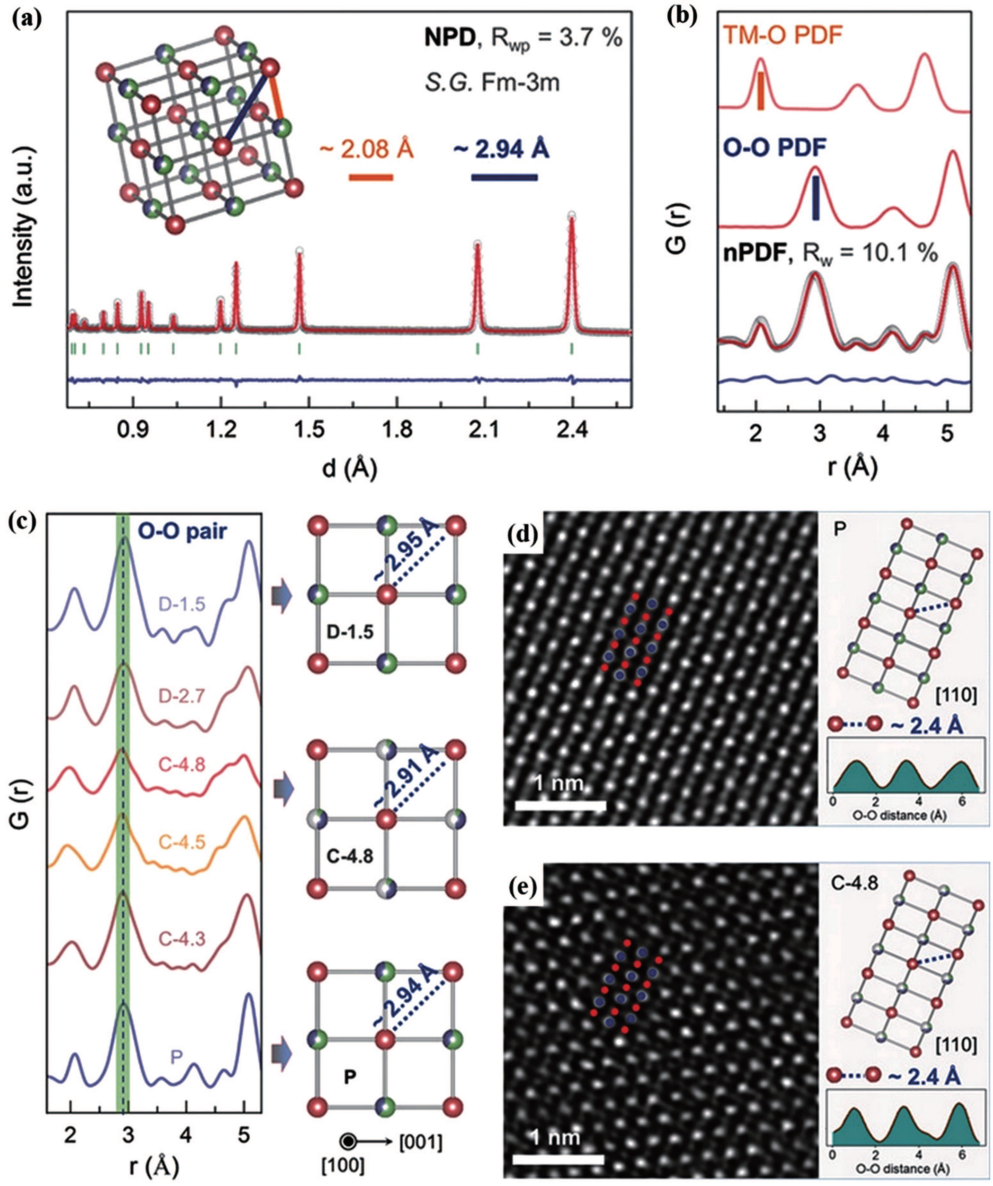


Fig. 6. $Li_xTi_{0.35}Ni_{0.35}Nb_{0.1}O_{1.8}F_{0.2}$ refinement results of the (a) neutron powder diffraction with its crystal structure shown in the inset, and (b) neutron PDF patterns with atom pair distance and corresponding PDF peaks labeled. (c) The *ex-situ* local neutron PDF patterns (left panel), and variation of the average O–O distance (right panel). [110] STEM-HAADF images of the (d) pristine and (e) 4.8 V charged samples, the corresponding average distances of the nearest-neighbor O–O columns projected along the [110] axis are labeled in the structure schematic.[55]

3.3. Hidden short-range order in battery materials

High voltage spinel $LiNi_{0.5}Mn_{1.5}O_4$ has high operating voltage ($\sim$ 4.75 V) and therefore high energy density. For a long time, it was believed that this material is either 'disordered' or 'ordered'. The disordered phase features Ni and Mn randomly occupying the 16d crystallographic site in the structure described by space group $Fd\bar{3}m$. The ordered phase features Ni/Mn ordering (Ni occupying 4b site and Mn occupying 12d site) in the structure described by space group $P4_332$.[56–58] XRD is typically used to identify the nature of

$LiNi_{0.5}Mn_{1.5}O_4$ phase. The XRD of the disordered phase lacks super lattice peaks associated with Ni/Mn ordering that is observed in the XRD of the ordered phase. Such belief is strongly questioned by nPDF study done by Liu *et al.*[59] The results suggest Ni/Mn ordering persists in both disordered and ordered phases. But such local ordering may or may not form corporately leading to long-range order. Specifically, figure 7 shows the nPDF data of four $LiNi_{0.5}Mn_{1.5}O_4$ samples synthesized under different conditions. Two nonannealed samples (FC and SC) were identified as disordered phase and two annealed samples (A48 and A240) crystallized in ordered phase. Though the atomic pair correlations in the four samples are quite different from each other in the long-range (> 5 Å), the PDF data sets of the four samples below 5 Å are remarkably similar. The almost identical PDF character in short-range indicates that the local structures are indistinguishable in the four samples. Figure 7(b) displays the atomic structure and Ni/Mn arrangements in the ordered phase. It is clear that 5 Å is the typical distance between the second nearest Ni/Mn neighbors. The authors accordingly proposed that up to the second nearest coordination shell the cations arrangements in the disordered phase are actually the same as those in the ordered phase. The refinement of nPDF results is shown in Fig. 7(c). Clearly, for the disordered phase, the local order gradually grows into long-range disorder as the atomic pair distance increases. This result overturns the traditional impression on the Ni/Mn ordering schemes in $LiNi_{0.5}Mn_{1.5}O_4$ materials and suggests that Ni/Mn ordering domain size is a more important factor than the degree of Ni/Mn mixing that affects the electrochemical performances of the material.

Another example of how nPDF reveals the existence of short-range ordering is the study on $LiNi_{0.5}Mn_{0.5}O_2$ material. Breger *et al.* found that strong site occupation correlation exists between Ni and Mn cations in the first and the second coordination shells which leads to non-random distribution in the short-range.[23] The conclusion is drawn through a reverse Monte–Carlo (RMC) type simulation of the PDF data. An RMC simulation of PDF data is done in a "big box" structure model containing hundreds to thousands of atoms by constantly swapping and moving atoms until the normalized difference between calculated PDF data and measured PDF data stays invariant or smaller than criteria set by the user.[60,61] Extensive contents about RMC methods and other PDF data analysis techniques can be found in previous reviews.[62,63] Figures 8(a) and 8(b) show the fitting results of PDF data using a "small box" model with randomly distributed cations and the fitting results of PDF data after RMC simulation using a "big box" model, respectively. It is clear that the RMC simulation improved the fitting results significantly, especially in the short distance region. Detailed analysis of the structure model after RMC simulation revealed several hidden short-range ordering features. One is that the Ni cations tend to be surrounded by more Mn cations in the first coordination shell and more Li and Ni cations in the second shell. Another structural feature is that about 10% Li/Ni mixing exists which means about 10% of Li ions from the Li layer exchange with Ni cations in the transition metal layer. Furthermore, the Li ions in the transition meal layer try to avoid Ni cations in their first coordination shell and tend to be surrounded by Mn cations. These results on the local structural feature cannot be captured by the average structural model from fitting to diffraction data. Combining PDF data and advanced fitting/simulation methods could open our access to much enriched structural information for battery-related material researches.

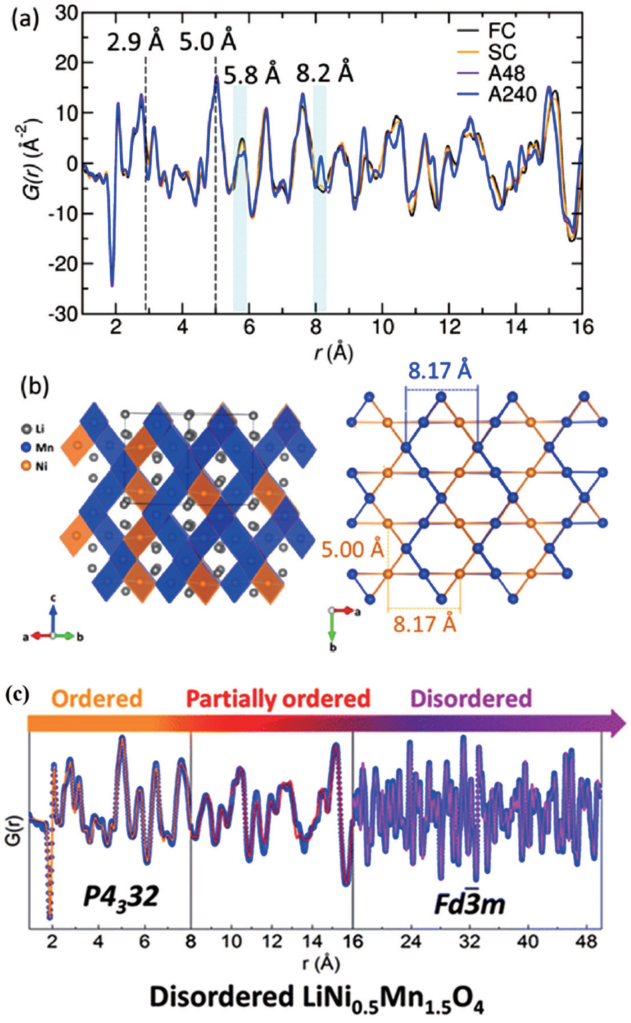


Fig. 7. (a) Neutron PDF data of annealed A48 (annealed for 48 h) and A240 (annealed for 240 h) and nonannealed FC (fast cooled) and SC (slow cooled) $LiNi_{0.5}Mn_{1.5}O_4$ samples. (b) Structure of the ordered[7] $LiNi_{0.5}Mn_{1.5}O_4$ (S.G. $P4_332$) polymorph viewed along the [110] direction. All oxygen atoms are omitted for clarity. (c) Least-squares refinements of the disordered (S.G. $Fd\bar{3}m$) and ordered (S.G. P_4332) structure models using local PDF data of the disordered $LiNi_{0.5}Mn_{1.5}O_4$ sample, which has local Ni/Mn ordering in the short-range (agrees well with the ordered model), and long-range Ni/Mn disordering (agrees well with the disordered model).[59]

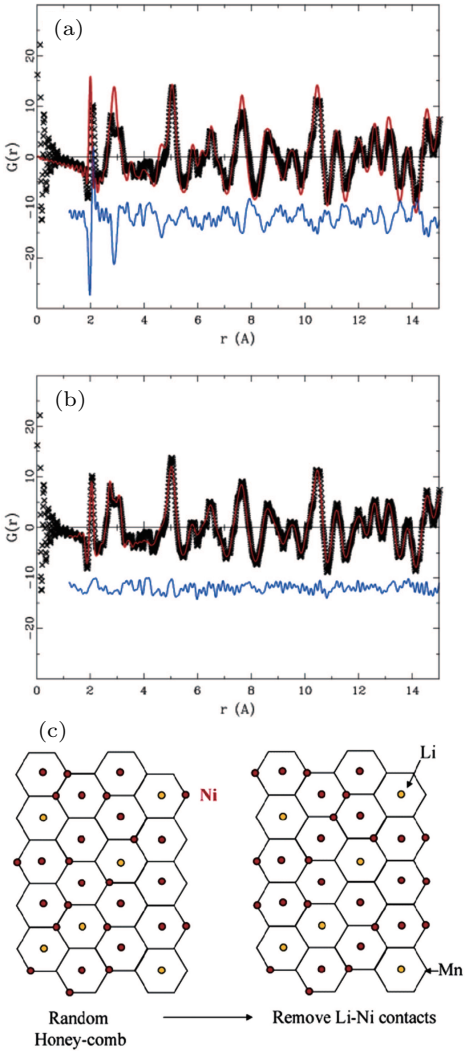


Fig. 8. Reverse Monte–Carlo simulation results for pristine[7] $LiNi_{0.5}Mn_{0.5}O_2$: (a) the fitting results by using the initial random cluster model, and (b) the fitting results after the RMC calculations. Black crosses: experimental data, solid red line: calculated PDF, blue line: difference between the calculated and experimental patterns. (c) The transition metal layers for $LiNi_{0.5}Mn_{0.5}O_2$ with 10% of Li/Ni site exchange are represented by honeycomb, within which the atoms are distributed randomly. Yellow circles: Li atoms; red circles: Ni atoms; corners without circles: Mn.[23]

4. Summary and perspectives

As a total scattering technique, PDF is not limited to long-range order and capable of probing both crystalline and amorphous phases. For battery materials, PDF is particularly effective in studying nano or amorphous materials such as silicon anode and conversion cathode; the local probe capability of PDF coupled with high oxygen sensitivity of neutron makes nPDF an ideal tool for studying anion redox reactions; PDF can also reveal the subtle short-range structural information that is difficult to characterize otherwise. Like any other characterization technique, the results from PDF analysis are more convincing when they are consistent with information obtained from different methods such as imaging, spectroscopy, and theoretical simulation. For example, in the study on conversion material $Fe_{0.9}Co_{0.1}OF$, the particle size and phase distribution information obtained from PDF analysis was verified by TEM.[49] In another study, Lyu *et al.* identified the presence of Ru–Ru metal bonding in $Li_2Ru_{0.5}Mn_{0.5}O_3$ materials through PDF technique and such structural feature was later found in TEM.[35] In studying $CuMn_2O_4$ which is not a battery material, Shoemaker *et al.* used RMC to analyze the PDF result and found the occurrence of Cu^{3+}. Such occurrence was independently verified by x-ray photoelectron spectroscopy data.[64]

When it comes to combing PDF with computational chemical methods such as density functional theory (DFT) calculation and molecular dynamics (MD) simulation, more detailed information at atomic scale can be obtained. Functions such as RDF can be directly computed from the structural models used in DFT and MD calculations statistically and compared with the results from PDF experiments. With such approach, PDF has helped revealing solvation environment and diffusion pathways of Li ions for many liquid/solid electrolyte materials.[30,65] However, the combination between theoretical calculation and PDF can sometimes be challenging considering that PDF study commonly involves a large unit cell which can be costly in terms of computation resources.

On the one hand, the importance of PDF is increasingly recognized by the battery community. On the other hand, PDF experiment is far from routine as it generally requires high energy and high flux radiation sources. Fortunately, the situation is getting better as more and more x-ray synchrotron facilities and neutron sources are being built around the world. A wider application of PDF to battery materials is expected and more interesting science is to be found.[52,53]

Acknowledgment

The work done at Brookhaven National Laboratory was supported by the Assistant Secretary for Energy Efficiency and Renewable Energy, Vehicle Technology Office of the U.S. DOE through the Advanced Battery Materials Research (BMR) Program, including Battery500 Consortium under contract No. DE-SC0012704.

References

[1] Larcher D and Tarascon J M 2015 *Nat. Chem.* **7** 19
[2] https://www.nobelprize.org/prizes/chemistry/ 2019/press-release/
[3] Hu E, Wang X, Yu X and Yang X Q 2018 *Acc. Chem. Res.* **51** 290
[4] Rong X, Hu E, Lu Y, Meng F, Zhao C, Wang X, Zhang Q, Yu X, Gu L, Hu Y S, Li H, Huang X, Yang X Q, Delmas C and Chen L 2019 *Joule* **3** 503
[5] Hu E, Bak S M, Liu J, Yu X, Zhou Y, Ehrlich S N, Yang X Q and Nam K W 2014 *Chem. Mater.* **26** 1108
[6] Zhou Y N, Ma J, Hu E, Yu X, Gu L, Nam K W, Chen L, Wang Z and Yang X Q 2014 *Nat. Commun.* **5** 5381
[7] Liu D, Shadike Z, Lin R, Qian K, Li H, Li K, Wang S, Yu Q, Liu M, Ganapathy S, Qin X, Yang Q H, Wagemaker M, Kang F, Yang X Q and Li B 2019 *Adv. Mater.* **31** 1806620
[8] Zhu H, Huang Y, Zhu H, Wang L, Lan S, Xia X and Liu Q 2019 *Small Methods* 1900223

[9] Liang G, Didier C, Guo Z, Pang W K and Peterson V K 2019 *Adv. Mater.* 1904528
[10] Li L, Xie Y, Maxey E and Harder R 2019 *J. Synchrotron Radiat.* **26** 220
[11] Ren Y and Zuo X 2018 *Small Methods* **2** 1800064
[12] Jung W I, Nagao M, Pitteloud C, Itoh K, Yamada A and Kanno R 2009 *J. Mater. Chem.* **19** 800
[13] Laveda J V, Johnston B, Paterson G W, Baker P J, Tucker M G, Playford H Y, Jensen K M Ø, Billinge S J L and Corr S A 2018 *J. Mater. Chem. A* **6** 127
[14] Zhu H, Li Q, Ren Y, Fan L, Chen J, Deng J and Xing X 2016 *Adv. Mater.* **28** 6894
[15] Zhu H, Li Q, Yang C, Zhang Q, Ren Y, Gao Q, Wang N, Lin K, Deng J, Chen J, Gu L, Hong J and Xing X 2018 *J. Am. Chem. Soc.* **140** 7403
[16] Hua X, Robert R, Du L S, Wiaderek K M, Leskes M, Chapman K W, Chupas P J and Grey C P 2014 *J. Phys. Chem. C* **118** 15169
[17] Hu Y Y, Liu Z, Nam K W, Borkiewicz O J, Cheng J, Hua X, Dunstan M T, Yu X, Wiaderek K M, Du L S, Chapman K W, Chupas P J, Yang X Q and Grey C P 2013 *Nat. Mater.* **12** 1130
[18] Bréger J, Kang K, Cabana J, Ceder G and Grey C P 2007 *J. Mater. Chem.* **17** 3167
[19] Pigliapochi R, Seymour I D, Merlet C, Pell A J, Murphy D T, Schmid S and Grey C P 2018 *Chem. Mater.* **30** 817
[20] Zeng D, Cabana J, Bréger J, Yoon W S and Grey C P 2007 *Chem. Mater.* **19** 6277
[21] Zhang M J, Teng G, Chen-Wiegart Y K, Duan Y, Ko J Y P, Zheng J, Thieme J, Dooryhee E, Chen Z, Bai J, Amine K, Pan F and Wang F 2018 *J. Am. Chem. Soc.* **140** 12484
[22] Ma J, Bo S H, Wu L, Zhu Y, Grey C P and Khalifah P G 2015 *Chem. Mater.* **27** 2387
[23] Bréger J, Dupré N, Chupas P J, Lee P L, Proffen T, Parise J B and Grey C P 2005 *J. Am. Chem. Soc.* **127** 7529
[24] Zhang Z, Zhang M, Wang Y, Tan Q, Lv X, Zhong Z, Li H and Su F 2013 *Nanoscale* **5** 5384
[25] Lee J H, Kim W J, Kim J Y, Lim S H and Lee S M 2008 *J. Power Sources* **176** 353
[26] Allan P K, Griffin J M, Darwiche A, Borkiewicz O J, Wiaderek K M, Chapman K W, Morris A J, Chupas P J, Monconduit L and Grey C P 2016 *J. Am. Chem. Soc.* **138** 2352
[27] Krauskopf T, Culver S P and Zeier W G 2018 *Chem. Mater.* **30** 1791
[28] Lin R, Hu E, Liu M, Wang Y, Cheng H, Wu J, Zheng J C, Wu Q, Bak S, Tong X, Zhang R, Yang W, Persson K A, Yu X, Yang X Q and Xin H L 2019 *Nat. Commun.* **10** 1650
[29] Narten A H, Vaslow F and Levy H A 1973 *J. Chem. Phys.* **58** 5017
[30] Ohara K, Mitsui A, Mori M, Onodera Y, Shiotani S, Koyama Y, Orikasa Y, Murakami M, Shimoda K, Mori K, Fukunaga T, Arai H, Uchimoto Y and Ogumi Z 2016 *Sci. Rep.* **6** 21302
[31] Shadike Z, Lee H S, Tian C, Sun K, Song L, Hu E, Waluyo I, Hunt A, Ghose S, Hu Y, Zhou J, Wang J, Northrup P, Bak S M and Yang X Q 2019 *Adv. Energy Mater.* **9** 1900705
[32] Sławiński W A, Playford H Y, Hull S, Norberg S T, Eriksson S G, Gustafsson T, Edström K and Brant W R 2019 *Chem. Mater.* **31** 5024
[33] Uhlig H, Hoffmann M J, Lamparter H P, Aldinger F, Bellissent R and Steeb S 1996 *J. Am. Ceram. Soc.* **79** 2833
[34] Zhao E, He L, Wang B, Li X, Zhang J, Wu Y, Chen J, Zhang S, Liang T, Chen Y, Yu X, Li H, Chen L, Huang X, Chen H and Wang F 2019 *Energy Storage Mater.* **16** 354
[35] Lyu Y, Hu E, Xiao D, Wang Y, Yu X, Xu G, Ehrlich S N, Amine K, Gu L, Yang X Q and Li H 2017 *Chem. Mater.* **29** 9053
[36] Debye P 1915 *Ann. Phys.* **351** 809
[37] Zernike F and Prins J A 1927 *Z. Phys. A Hadrons Nuclei* **41** 184
[38] Keen D A 2001 *J. Appl. Crystallogr.* **34** 172
[39] Chapman K W 2016 *MRS Bull.* **41** 231
[40] Radhakrishnan A N, Rao P P, Linsa K S, Deepa M and Koshy P 2011 *Dalton Trans.* **40** 3839
[41] Liu H, Chen Y, Hy S, An K, Venkatachalam S, Qian D, Zhang M and Meng Y S 2016 *Adv. Energy Mater.* **6** 1502143
[42] Nagler S E, Stoica A D, Stoica G M, An K, Skorpenske H D, Rios O, Hendin D B and Bower N W 2019 *J. Anal. Methods. Chem.* 6164058
[43] Billinge S J L 2019 *Philos Trans. A Math. Phys. Eng. Sci.* **377** 20180413
[44] Li H, Huang X, Chen L, Zhou G, Zhang Z, Yu D, Jun Mo Y and Pei N 2000 *Solid State Ion.* **135** 181
[45] Aric A S, Bruce P, Scrosati B, Tarascon J M and Van Schalkwijk W 2010 *Materials for Sustainable Energy* (London: Co-Published with Macmillan Publishers Ltd) pp. 148–159
[46] Key B, Morcrette M, Tarascon J M and Grey C P 2011 *J. Am. Chem. Soc.* **133** 503
[47] Li L, Meng F and Jin S 2012 *Nano Lett.* **12** 6030
[48] Wiaderek K M, Borkiewicz O J, Castillo-Martinez E, Robert R, Pereira N, Amatucci G G, Grey C P, Chupas P J and Chapman K W 2013 *J. Am. Chem. Soc.* **135** 4070
[49] Fan X, Hu E, Ji X, Zhu Y, Han F, Hwang S, Liu J, Bak S, Ma Z, Gao T, Liou S C, Bai J, Yang X Q, Mo Y, Xu K, Su D and Wang C 2018 *Nat. Commun.* **9** 2324
[50] Sathiya M, Rousse G, Ramesha K, Laisa C P, Vezin H, Sougrati M T, Doublet M L, Foix D, Gonbeau D, Walker W, Prakash A S, Ben Hassine M, Dupont L and Tarascon J M 2013 *Nat. Mater.* **12** 827
[51] McCalla E, Sougrati M T, Rousse G, Berg E J, Abakumov A, Recham N, Ramesha K, Sathiya M, Dominko R, Van Tendeloo G, Novák P and Tarascon J M 2015 *J. Am. Chem. Soc.* **137** 4804
[52] Li B and Xia D 2017 *Adv. Mater.* **29** 1701054
[53] Saubanère M, McCalla E, Tarascon J M and Doublet M L 2016 *Energy Environ. Sci.* **9** 984
[54] Rong X, Liu J, Hu E, Liu Y, Wang Y, Wu J, Yu X, Page K, Hu Y S, Yang W, Li H, Yang X Q, Chen L and Huang X 2018 *Joule* **2** 125
[55] Zhao E, Li Q, Meng F, Liu J, Wang J, He L, Jiang Z, Zhang Q, Yu X, Gu L, Yang W, Li H, Wang F and Huang X 2019 *Angew. Chem. Int. Ed. Engl.* **58** 4323
[56] Idemoto Y, Narai H and Koura N 2003 *J. Power Sources* **119–121** 125
[57] Zhong Q, Bonakdarpour A, Zhang M, Gao Y and Dahn J R 1997 *J. Electrochem. Soc.* **144** 205
[58] Kim J H, Myung S T, Yoon C S, Kang S G and Sun Y K 2004 *Chem. Mater.* **16** 906
[59] Liu J, Huq A, Moorhead-Rosenberg Z, Manthiram A and Page K 2016 *Chem. Mater.* **28** 6817
[60] Farrow C L, Juhas P, Liu J W, Bryndin D, Božin E S, Bloch J, Proffen T and Billinge S J L 2007 *J. Phys.: Condens. Matter* **19** 335219
[61] McGreevy R L 2001 *J. Phys.: Condens. Matter* **13** R877
[62] Playford H Y, Owen L R, Levin I and Tucker M G 2014 *Annu. Rev. Mater. Res.* **44** 429
[63] Proffen T and Kim H 2009 *J. Mater. Chem.* **19** 5078
[64] Shoemaker D P, Li J and Seshadri R 2009 *J. Am. Chem. Soc.* **131** 11450
[65] Fujii K, Matsugami M, Ueno K, Ohara K, Sogawa M, Utsunomiya T and Morita M 2017 *J. Phys. Chem. C* **121** 22720